Extended FOGI-FLL Based Seamless Control of Grid Synchronized BES-PV Fed Water Pump System

Mohd. Kashif and Bhim Singh, *Fellow, IEEE*

***Abstract*—A battery energy storage and photovoltaic array powered grid-connected water pump system (WPS) becomes an island during outage of the grid. On the grid recovery, it is necessary to synchronize WPS to the grid to achieve advantages of grid-integration like increased system utilization and prolonged water pumping. Hence, a frequency locked-loop (FLL) based on extended fourth-order generalized integrator (eFOGI) to facilitate reconnection of WPS to the grid is developed in this article. The developed eFOGI-FLL eliminates dc-offset along with dominant low-order harmonics unlike existing generalized integrator-based FLL. The eFOGI-FLL, consisting of two cascaded notch-filters, is tuned to fundamental, fifth and seventh harmonic frequencies, and thus, it passes fundamental component and blocks two harmonics. Besides, eFOGI-based quadrature signal generator (QSG) is used to implement control for grid-interfaced converter in grid-connected and islanded modes. While eFOGI-QSG-based sensorless control of permanent magnet synchronous motor, which is used to operate WPS, is also developed to eliminate position sensor. The benefits of eFOGI-FLL are highlighted by performing its in-depth analysis. Experimental behavior of WPS in several operating scenarios are reported to show effectiveness of developed control techniques.**

***Index Terms*—Extended fourth-order generalized integrator (EFOGI), frequency locked loop (FLL), grid, photovoltaic (PV) array, synchronization, water pump system (WPS).**

I. Introduction

With the reducing cost of solar photovoltaic (PV) technology, for instance 80% cost reduction in previous decade, the increasing impacts of climate change like droughts, floods, etc. and the necessity to setup low-carbon energy transition, PV array fed systems are gaining popularity due to their versatility towards several crucial applications, such as solar water pumping (SWP) [1]. SWP system (SWPS) increases agricultural yield and provides access to drinking water, which thereby improves users' financial health, and reduces water borne diseases [2]. Besides, such systems accelerate farmers' resilience against climate shocks like delusive rainfall patterns and droughts. However, an intermittency of solar irradiation severely influences utilization and water discharge rate of SWPS.

Manuscript received 16 April 2023; revised 4 July 2023 and 26 August 2023; accepted 26 September 2023. Date of publication 11 October 2023; date of current version 6 December 2023. This work was supported under Grants viz. RP03222-UAY, RP03128, and RP03195G, and in part by the SERB-NSC Fellowship. Recommended for publication by Associate Editor L. Peng. *(Corresponding author: Mohd. Kashif.)*

The authors are with the Department of Electrical Engineering, Indian Institute of Technology Delhi, New Delhi 110016, India (e-mail: mkashif19r@gmail.com; bsingh@ee.iitd.ac.in).

Color versions of one or more figures in this article are available at https://doi.org/10.1109/TPEL.2023.3323864.

Digital Object Identifier 10.1109/TPEL.2023.3323864

Although the inclusion of battery energy storage (BES) and water storage tank are presented in [3] and [4] to deal with above issue, these solutions increase system cost. Besides, former alternative has marginal impact on system utilization due to its limited-energy capacity, while later alternative demands considerable amount of land. Recently, a low-cost solution to enhance utilization while achieving steady water discharge is presented in [5], [6], and [7] through integration of SWPS to the utility grid. Nevertheless, SWPS turns into an island in the event of grid outage, and continues to operate in the islanded mode (IM) even after recovery of the utility grid. This is due to the absence of synchronization unit (SynU) from the system. Thus, it is essential to include this unit in the system to get advantages of grid integration. The SynU is a crucial part of system as it decides and executes reconnection of SWPS with the grid, which thereby realizes the interoperability and interconnection between the two such that both of them function efficiently [8].

Several schemes to implement grid synchronization have been developed in the literature [9], [10], [11], [12], [13], [14], [15], [16], [17], [18], [19], [20], [21], [22], [23], [24], [25]. The synchronous reference frame (SRF) based phase-locked loop (PLL) is among the popular schemes for three phase systems due to its ease of realization [9]. However, harmonics and dc-offset affect its performance significantly [10]. To deal with this issue, several solutions based on moving-average filter [11], adaptive notch filter (ANF) [12], all-pass filter [13], and delayed signal cancellation [14] are presented in the literature to improve the immunity of SRF-PLL against such disturbances.

Another method based on the concept of frequency-locking is developed for synchronization in [15], [16], [17], [18], [19], [20], [21], [22], [23], [24], [25]. The advantage of this frequency-locked loop (FLL) method over PLL scheme is that the sudden changes in the phase-angle of input voltage does not affect its performance [15]. Another advantage is that there is no voltage-controlled oscillator in FLL, unlike PLL, which thereby offers the versatility in optimizing FLL implementation by using cost-effective computational devices [16]. It is worth noting that main component in realization of majority of FLLs is the generalized integrator (GI), which is a double-integral structure that presents high gain at cut-off frequency, and works as an amplitude integrator of its input signal [17]. The second-order GI (SOGI) and ANF are two well-known GI-based FLL schemes that give an estimation of frequency, amplitude and phase of the input voltage [18], [19]. In addition to this, they provide an estimation of in-phase and quadrature components of the input voltage. Nevertheless, the existence of harmonics and

dc-offset in input voltage distorts estimated parameters. To deal with this issue, the prefiltering and in-loop filtering concepts as developed in [17], [20], and [21] are applied to SOGI-FLL. To implement pre-filtering, a band-pass filter (BPF) in the form of SOGI-based quadrature-signal generator (QSG) is introduced before the SOGI-FLL wherein the cut-off frequency of BPF is adapted on the basis of frequency variations by using FLL. Similarly, the in-loop filtering is realized by placing SOGI-QSG-based BPF inside the control loop of SOGI-FLL. In spite of rejecting dc-offset and reducing magnitude of harmonics, these two approaches do not result in harmonics elimination. Another method using third-order GI (TOGI) based FLL as presented in [22] provides dc-offset rejection and harmonic attenuation. Nonetheless, individual harmonic elimination is not realized. Although fourth-order GI (FOGI) based FLL rejects dc-offset and provides better attenuation than TOGI-FLL as described in [23], the property of rejecting harmonics selectively is still not achieved. Meanwhile, numeric algorithms [24], [25] and optimization-based methods [26], [27] have been proposed in the literature to eliminate harmonics selectively. These techniques loss their attractiveness as numeric algorithms are heavily dependent on initial values while optimization algorithms are devoid of mathematical theories and are susceptible to uncertainties in input parameters [25], [27].

Based on the motivation from in-loop filtering concept, and utilizing exemplary harmonic extraction property of ANF, the functionality of FOGI-based FLL is extended in this article by introducing two cascaded ANFs in its control-loop, thereby facilitating selective harmonic rejection. Hence, the developed structure is termed as extended FOGI-FLL (eFOGI-FLL). The cascaded ANFs eliminate two-dominant low-order harmonics from the three-phase system, viz. the seventh and fifth harmonics as these structures are tuned to respective harmonic frequency. This benefit is obtained by passing the α- (or, β-) axis error of eFOGI-FLL through two cascaded ANFs wherein first and second units, respectively eliminate 7th and 5th harmonic components. The α- (or, β) axis error signal is produced through comparison of α- (or, β-) axis grid voltages with α- (or, β-) axis eFOGI-FLL based in-phase component.

Subsequently, the developed eFOGI-FLL is used to realize seamless reconnection of PV-BES powered water pump system (WPS) with the grid, which thereby secures the advantages of the grid integration, namely, enhanced system utilization and prolonged water pumping. A comparison of presented and existing synchronization techniques, is given in Table I. It is noteworthy that the system is operated in an IM in the event of grid outage and presented eFOGI-FLL is used to reconnect WPS with the grid when the utility grid is recovered. This realizes operation of the system in grid connected mode (GCM). Besides, eFOGI-based QSG is used to implement the control for grid-interfaced voltage source converter (GVSC). This maintains power quality at grid terminals as per the IEEE-519 standard. Even, the maximum power control (MPC) of a PV array is also realized in GVSC control, thereby eliminating a need for boost dc–dc converter-based MPC. Consequently, PV array terminals are directly connected to the dc-link, and thus this results in cost reduction. Meanwhile, a BES is also integrated in the system,

TABLE I
COMPARISON OF PRESENTED EFOGI-FLL WITH EXISTING SYNCHRONIZATION TECHNIQUES

Synchronization Scheme	Merits	Demerits
Complex Band Pass Filter FLL [1]	Good Harmonic Attenuation	Sluggish Dynamic Performance
Adaptive Transfer Delay FLL [2]	Fast Transient Response	Poor Harmonic Attenuation
Circular Limit-cycle Oscillator-Based FLL [3]	Simple Realization	Poor Harmonic Attenuation
Limit Cycle Oscillator FLL [4]	Simple Realization	Poor Harmonic Attenuation
Comb-FLL [5]	Good Harmonic Attenuation	Complex Realization
SOGI-FLL [6]	Simple Realization	Poor Harmonic/DC-offset Elimination
FOGI-FLL [7]	DC-offset Elimination	Poor Harmonic Elimination
Presented eFOGI-FLL	Selective Harmonic /DC-offset Rejection	Complex Realization

which helps in realizing uninterrupted operation of WPS in an IM. Besides, developed eFOGI-QSG is utilized to implement self-sensing control for permanent magnet synchronous motor, which removes mechanical sensor from PMSM-drive. Thus, major contributions of this article are as follows.

1) Realization of eFOGI-FLL for rejecting DC offset and lower order harmonic components, viz. seventh and fifth.
2) Development of eFOGI-FLL-based controls to synchronize PV-BES fed WPS to the utility grid.
3) Realization of eFOGI-QSG-based GVSC control to operate system under both GCM and IM.

It is worth noting that other applications of developed eFOGI-FLL are synchronization of microgrid [28], wind energy conversion system [29], hydroenergy conversion system [30], fuel cell-based system [31], and tidal energy conversion system [32] with the utility grid. Meanwhile, remaining sections of this article are categorized as follows. In Section II, a layout of system is presented. While different control techniques including eFOGI-QSG-based GVSC control and eFOGI-FLL-based seamless control for grid synchronization are described in Section III. Besides, in Section IV, experimental behavior of WPS in different operating states are acquired. Finally, Section V concludes this article.

II. SYSTEM LAYOUT

The conceptual diagram of PV-BES fed grid-synchronized WPS is depicted in Fig. 1. The power electronic interface of the system is integrated to utility grid through the SynU. In addition to grid, the PV array and BES are other two energy resources. BES is used to deliver constant power to loads under utility grid outage. Besides, PMSM-pump unit and local-loads present the total load-demand of the system where the local-loads represent miscellaneous loads of WPS like pressure boosters, cooling fans and others. While the control-unit sends signals to power electronic interface, thereby controlling power flow through different system components.

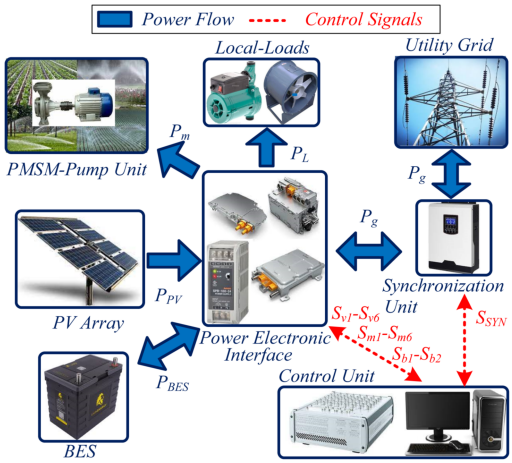

Fig. 1. Concept of PV array and BES powered grid interfaced WPS with provision to deliver local loads.

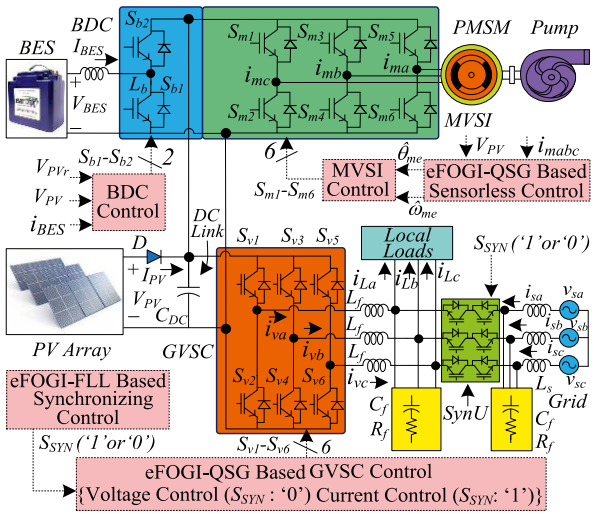

Fig. 2. Schematics of grid synchronized PV-BES fed WPS.

Likewise, the control signal, S_{SYN} governs the operation of SynU, which thereby decides the reconnection /disconnection of system to/from the utility grid.

Besides, the high-level block diagram of WPS illustrating major components of system and flow of power among them, is depicted in Fig. 2. The insulated-gate bipolar junction transistor-based bidirectional switches are used to realize SynU as noted from figure. Based on logic "0"/logic "1" status of S_{SYN}, SynU disconnects/reconnects WPS from/to the grid. Besides, GVSC control is switched between current and voltage controls based on the status of S_{SYN} where logic "1" activates current control and logic "0" activates voltage control. While PV array is interfaced across the dc-link as its MPC is implemented in GVSC control. Thus, there is no need to use a boost converter for MPC of a PV array. Meanwhile, a bidirectional converter (BDC) is used to interface BES at dc link. Additionally, self-sensing control of PMSM based on presented eFOGI-QSG is implemented to remove position sensor, thereby increasing reliability and reducing cost of system. The PMSM-pump unit is operated by using machine-side voltage source inverter (MVSI) as noted from figure. The key features of IM as well as GCM are given in Table II. Besides, the specifications of key components of WPS are given in Table III.

TABLE II
KEY FEATURES OF GRID CONNECTED AND ISLANDED MODES

Parameter	Grid Connected Mode	Islanded Mode
Utility Grid	Present	Absent
Nature of GVSC Control	Current Control	Voltage Control
SynU Status	ON	OFF
BES Status	Discharging/Charging	Charging
Total Loads of System	BES + PMSM-pump set + Local-loads	PMSM-pump set + Local-loads
Energy Sources	Utility Grid + PV Array	BES + PV Array

TABLE III
RATINGS OF MAIN COMPONENTS OF SYSTEM

Components	Ratings
PMSM	220 V, 2200 W, 2 pole-pairs, 1500 r/min
Local-Loads	1 kW, 50 Hz, 220 V
PV Array	Voltage of PV-array in MPC, V_{PV} is calculated as, $V_{PV} = \sqrt{2/3}(2V_{line}/m_x) = \sqrt{2/3}(2\times 220/0.99) = 360V$ where, V_{line} = 220 V is PMSM line voltage, m_x = 0.99 is modulation index. Power of PV array in MPC, P_{PV} is selected as 3300 W. Thus, PV current in MPC, I_{PV} is deduced as, $I_{PV} = P_{PV}/V_{PV} = 3300/360 = 9.16\,A$
BES	Based on 8 h backup, BES energy capacity, EC_{BES} is obtained as, $EC_{BES} = (TLD).(BHrs) = 3.2kW\times 8h = 25.6\,kWh$ where, TLD = 3.2 kW is the total-load demand, $BHrs$ = 8 hrs is number of backup hours. BES nominal voltage is chosen as 240 V. The BES ampere-hour, AH_{BES} rating is given as, $AH_{BES} = EC_{BES}/V_{nBES} = 25.6kW/240V = 107\,Ah$

III. CONTROL OF SYSTEM

Both presented structures, viz. eFOGI-QSG and eFOGI-FLL are presented in this section. Besides, details of different control schemes including eFOGI-QSG-based GVSC control and eFOGI-FLL-based control for synchronization of WPS with utility grid are described in following subsections.

A. Presented eFOGI-QSG Structure

The presented eFOGI-QSG utilizes exemplary harmonic extraction property of ANF for rejection of two-dominant low-order harmonics. Hence, properties of ANF are discussed first in this subsection. Then, details of eFOGI-QSG are described.

On the basis of ANF structure as illustrated in Fig. 3(a), an expression of transfer function, H_{ANF} relating error signal, e_i to input signal, i is deduced as

$$H_{\mathrm{ANF}}(s) = \frac{e_i(s)}{i(s)} = \frac{s^2+\omega_c^2}{s^2+\omega_c k_1 s+\omega_c^2} \tag{1}$$

where ω_c is cut-off frequency, k_1 is the gain-term while "s" is Laplace operator. Based on (1), the frequency response of

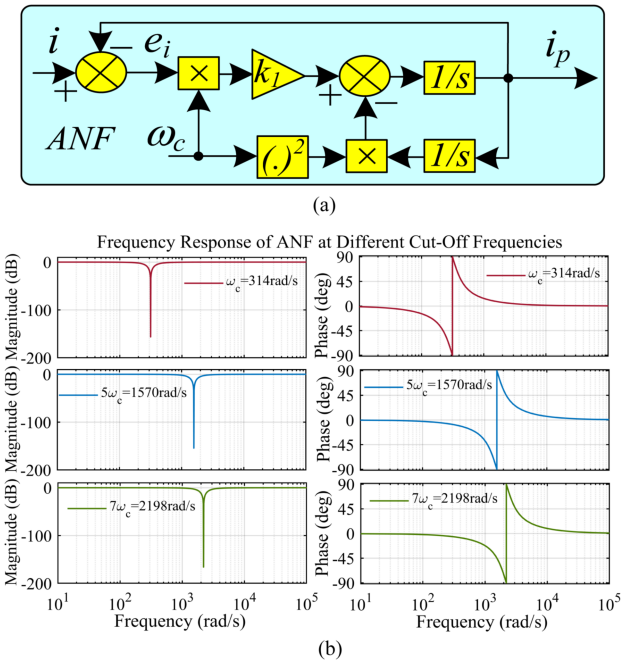

Fig. 3. (a) Adaptive notch filter and (b) its frequency response at $\omega_s = 314$ rad/s, $5\omega_s$, $7\omega_s$.

ANF for different cut-off frequencies is obtained as illustrated in Fig. 3(b). It is worth noting that ANF offers 0 dB gain at all frequencies except cut-off frequency, which means that it passes all frequency components except one corresponding to cut-off frequency. While the gain at cut-off frequency is quite large and negative, thereby indicating that ANF obstructs the signal corresponding to cut-off frequency. Besides, these two properties of ANF are obtained at different cut-off frequencies. Hence, using excellent harmonic filtering property of ANF, two cascaded ANFs are placed inside control-loop of FOGI, thereby realizing presented eFOGI-QSG as depicted in Fig. 4. The first ANF rejects fifth harmonic while second rejects the seventh harmonic as these ANFs are, respectively, tuned to fifth and seventh harmonics frequencies. From Fig. 4, the in-phase, H_{eFp}, and quadrature, H_{eFq} transfer functions eFOGI-QSG are deduced as

$$H_{eFp}(s) = \frac{i_{Lpa}(s)}{i_{La}(s)} = \frac{H_5\, H_7\, g_1\, g_2\, \omega_s^2\, s^2}{s^4+\omega_s g_1 s^3+(2+H_5H_7g_1g_2)\omega_s^2 s^2+\omega_s^3 g_1 s+\omega_s^4} \tag{2}$$

$$H_{eFq}(s) = \frac{i_{Lqa}(s)}{i_{La}(s)} = \frac{H_5\, H_7\, g_1\, g_2\, \omega_s^3\, s}{s^4+\omega_s g_1 s^3+(2+H_5H_7g_1g_2)\omega_s^2 s^2+\omega_s^3 g_1 s+\omega_s^4} \tag{3}$$

where ω_s is the fundamental grid frequency, g_1, g_2 are the gain terms while H_5 and H_7 are the transfer functions of ANFs, which are tuned to fifth and seventh harmonic frequencies. Expressions of H_5 and H_7 are given as

$$H_5(s) = \frac{s^2+(5\omega_s)^2}{s^2+(5\omega_s)k_1 s+(5\omega_s)^2} \tag{4}$$

$$H_7(s) = \frac{s^2+(7\omega_s)^2}{s^2+(7\omega_s)k_1 s+(7\omega_s)^2}. \tag{5}$$

From (2) and (3), the frequency responses of $H_{eFP}(s)$ and $H_{eFq}(s)$ are obtained as illustrated in Fig. 5. It is noteworthy that the following.

1) Fifth and seventh harmonics are rejected selectively by both $H_{eFP}(s)$ and $H_{eFq}(s)$.
2) Besides, both of these transfer functions reject dc-offset.
3) They even pass fundamental component without attenuation as the gain at fundamental frequency is 0 dB.
4) Meanwhile, $H_{eFP}(s)$ and $H_{eFq}(s)$ offer 0° and 90° phase-shift, respectively at fundamental frequency.

B. eFOGI-QSG Based Control for GVSC

The eFOGI-QSG-based control for GVSC in grid-connected and IMs is described in this section.

1) GVSC Control in Grid-Connected Mode (GCM): The block diagram of GVSC control in GCM is depicted in Fig. 6. To produce switching pulses for GVSC in GCM, the unit-templates (u_{pc}, u_{pb}, u_{pa}) and total weighting-factor (w_T) are needed. Thus, the unit-templates are produced as

$$u_{pa} = (v_{sa1}/\hat{V}_{sp})\ u_{pb} = (v_{sb1}/\hat{V}_{sp})\ u_{pc} = (v_{sc1}/\hat{V}_{sp}) \tag{6}$$

where v_{sa1}, v_{sb1}, v_{sc1} and u_{pa}, u_{pb}, u_{pc} are the fundamental grid voltages and unit-templates of phase a, phase b, phase c, and V_{sp} is the amplitude of estimated grid phase-voltage. The fundamental grid voltages are obtained by processing the three phase-voltages of grid through eFOGI-QSG as

$$v_{sa\,1}(s) = \frac{H_5\, H_7\, g_1\, g_2\, \hat{\omega}_s^2\, s^2}{s^4+\hat{\omega}_s g_1 s^3+(2+H_5H_7g_1g_2)\hat{\omega}_s^2 s^2+\hat{\omega}_s^3 g_1 s+\hat{\omega}_s^4} v_{sa}(s) \tag{7}$$

$$v_{sb1}(s) = \frac{H_5\, H_7\, g_1\, g_2\, \hat{\omega}_s^2\, s^2}{s^4+\hat{\omega}_s g_1 s^3+(2+H_5H_7g_1g_2)\hat{\omega}_s^2 s^2+\hat{\omega}_s^3 g_1 s+\hat{\omega}_s^4} v_{sb}(s) \tag{8}$$

$$v_{sc1}(s) = \frac{H_5\, H_7\, g_1\, g_2\, \hat{\omega}_s^2\, s^2}{s^4+\hat{\omega}_s g_1 s^3+(2+H_5H_7g_1g_2)\hat{\omega}_s^2 s^2+\hat{\omega}_s^3 g_1 s+\hat{\omega}_s^4} v_{sc}(s) \tag{9}$$

where "ˆ" represents estimated quantities; v_{sa}, v_{sb}, v_{sc} are three phase voltages of grid which are obtained from line-voltages as

$$v_{sa} = (2v_{sab} + v_{sbc})/3 \tag{10}$$

$$v_{sb} = (-v_{sab} + v_{sbc})/3 \tag{11}$$

$$v_{sc} = (-v_{sab} - 2v_{sbc})/3 \tag{12}$$

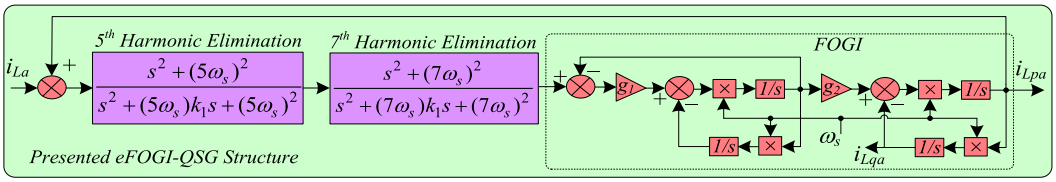

Fig. 4. Block diagram of presented eFOGI-QSG structure.

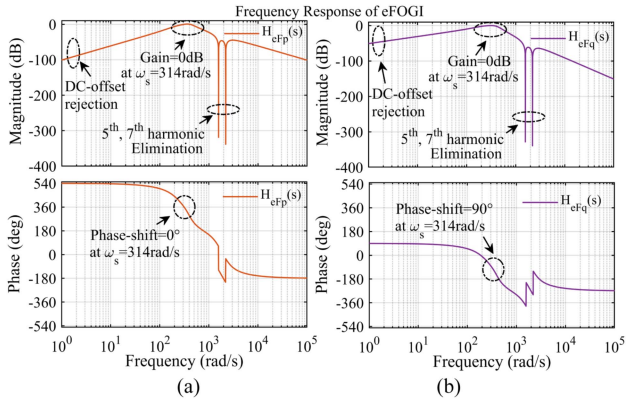

Fig. 5. Frequency response of eFOGI. (a) $H_{eFp}(s)$ and (b) $H_{eFq}(s)$.

where v_{sab} and v_{sbc} are the grid line-voltages. Then, total weighting factor, w_T is deduced as

$$w_T = w_{\text{BES}} + w_{\text{loss}} + w_{\text{PV}} + w_L \tag{13}$$

where w_{BES}, w_{loss}, w_{PV}, and w_L are BES, dc-loss, PV and local-load weighting factors. w_{BES}, w_{loss}, and w_{PV} are deduced as follows:

$$w_{\text{loss}} = (k_{sp} + k_{si}/s)(V_{\text{PV}r} - V_{\text{PV}}) \tag{14}$$

$$w_{\text{PV}} = \{2(P_{\text{PV}} - P_m)/(3\hat{V}_{sp})\} \tag{15}$$

$$w_{\text{BES}} = 2I_{\text{BES}}V_{\text{BES}}/(3\hat{V}_{sp}) \tag{16}$$

where $V_{\text{PV}r}$ and V_{PV} are the reference and sensed PV voltages; P_{PV} and P_m are PV and motor powers; V_{BES} and I_{BES} are BES voltage and current; and k_{sp} and k_{si} are PI-controller gains. The w_L is evaluated as follows:

$$w_L = (w_{La} + w_{Lb} + w_{Lc})/3 \tag{17}$$

where w_{La}, w_{Lb}, w_{Lc} are amplitudes of three-phase currents of local-loads, which are obtained by processing u_{pa}, u_{pb}, u_{pc} and eFOGI-QSG-based quadrature components of load currents ($i_{Lqa}, i_{Lqb}, i_{Lqc}$) through zero-crossing detector and sample-hold logics wherein i_{Lqa}, i_{Lqb}, i_{Lqc} are deduced as

$$i_{Lqa}(s) = \frac{H_5\, H_7\, g_1\, g_2\, \hat{\omega}_s^3\, s}{s^4 + \hat{\omega}_s g_1 s^3 + (2 + H_5 H_7 g_1 g_2)\hat{\omega}_s^2 s^2 + \hat{\omega}_s^3 g_1 s + \hat{\omega}_s^4} i_{La}(s) \tag{18}$$

$$i_{Lqb}(s) = \frac{H_5\, H_7\, g_1\, g_2\, \hat{\omega}_s^3\, s}{s^4 + \hat{\omega}_s g_1 s^3 + (2 + H_5 H_7 g_1 g_2)\hat{\omega}_s^2 s^2 + \hat{\omega}_s^3 g_1 s + \hat{\omega}_s^4} i_{Lb}(s) \tag{19}$$

$$i_{Lqc}(s) = \frac{H_5\, H_7\, g_1\, g_2\, \hat{\omega}_s^3\, s}{s^4 + \hat{\omega}_s g_1 s^3 + (2 + H_5 H_7 g_1 g_2)\hat{\omega}_s^2 s^2 + \hat{\omega}_s^3 g_1 s + \hat{\omega}_s^4} i_{Lc}(s). \tag{20}$$

Hence, based on the knowledge of u_{pc}, u_{pb}, u_{pa}, and w_T, the three-phase reference grid currents (i_{sar}, i_{sbr}, i_{scr}) are deduced as

$$i_{sar} = u_{pa} w_T,\ i_{sbr} = u_{pb} w_T,\ i_{scr} = u_{pc} w_T. \tag{21}$$

The three-phase grid currents are compared with their reference values and the resulting error is processed through hysteresis current controller, which thereby produces pulses for GVSC in GCM as depicted in Fig. 6. It is worth noting that proportional and integral gains of PI-controller are evaluated by using Ziegler–Nichols tuning rules [33], [34].

2) GVSC Control in IM: WPS operates in IM under the grid outage as per *qd*-based GVSC control as shown in Fig. 6. Using Park's transformation, *qd*-axes load voltages (V_{Lq}, V_{Ld}) are evaluated as follows:

$$\begin{bmatrix} V_{Lq} \\ V_{Ld} \end{bmatrix} = \frac{2}{3} \begin{bmatrix} -\sin\theta_{ud} & -\sin(\theta_{ud} - 2\pi/3) & -\sin(\theta_{ud} - 4\pi/3) \\ \cos\theta_{ud} & \cos(\theta_{ud} - 2\pi/3) & \cos(\theta_{ud} - 4\pi/3) \end{bmatrix} \begin{bmatrix} v_{La} \\ v_{Lb} \\ v_{Lc} \end{bmatrix} \tag{22}$$

where, v_{La}, v_{Lb}, v_{Lc} are three-phase load voltages, θ_{ud} is the updated load-angle, which is obtained by using phase-angle and frequency controller as discussed in Section III-D. While PI-controller is used to regulate these voltages as noted from Fig. 6. The output of PI-controller is chosen as reference *qd*-axes load currents (I_{Lqr}, I_{Ldr}). Thus, the reference load-currents (i_{Lar}, i_{Lbr}, i_{Lcr}) using inverse Park's transformation are obtained as follows:

$$\begin{bmatrix} i_{Lar} \\ i_{Lbr} \\ i_{Lcr} \end{bmatrix} = \begin{bmatrix} -\sin\theta_{ud} & \cos\theta_{ud} \\ -\sin(\theta_{ud} - 2\pi/3) & \cos(\theta_{ud} - 2\pi/3) \\ -\sin(\theta_{ud} - 4\pi/3) & \cos(\theta_{ud} - 4\pi/3) \end{bmatrix} \begin{bmatrix} I_{Lqr} \\ I_{Ldr} \end{bmatrix}. \tag{23}$$

The reference and sensed load currents as then used to produce switching pulses for GVSC in IM by using hysteresis current controller as illustrated in the figure.

C. Control of Bidirectional Converter

Fig. 7 depicts the control of BDC. The reference BES current, $I_{\text{BES}r}$ is constant under GCM (S_{SYN}: logical "1" status), and thus, BES is charged with a constant current when the grid

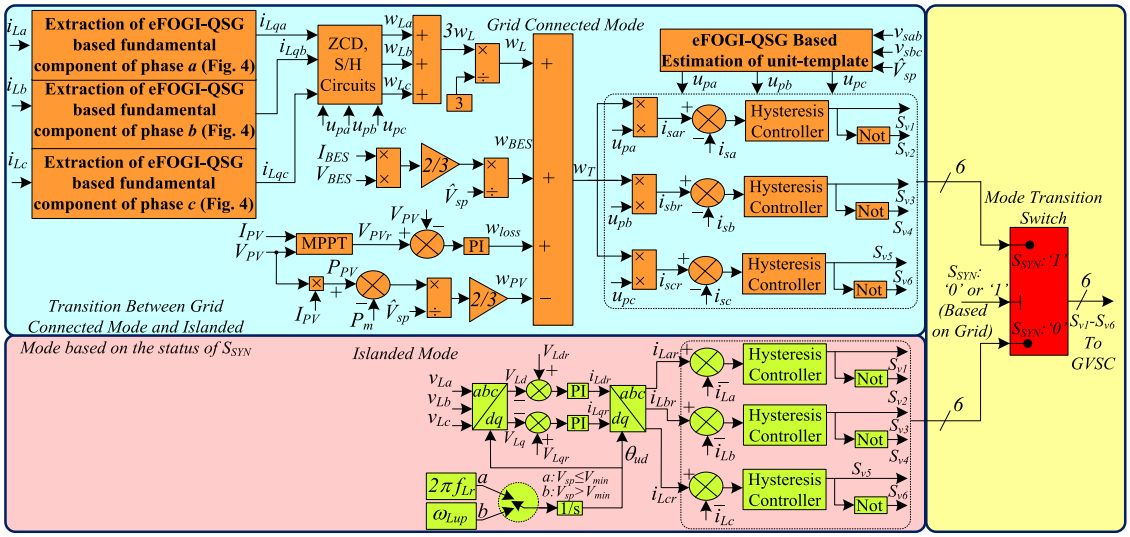

Fig. 6. Control for GVSC under GCM and IM.

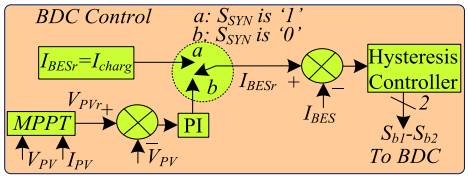

Fig. 7. Control for BDC.

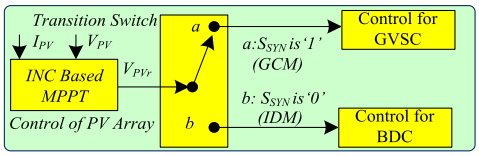

Fig. 8. Control of PV array.

is available. Under IM, $I_{\mathrm{BES}r}$ is obtained as an output of PI-controller as the dc-link voltage error is passed through it. It is worth noting that the reference PV array voltage is obtained from MPPT controller during IM. The reference and sensed BES currents are utilized by hysteresis controller for generation of switching signals for BDC.

D. Control of PV Array

The well-know incremental conductance algorithm is used for MPC of PV array [35]. It is worth noting that $V_{\mathrm{PV}r}$ is sent to GVSC controls when the status of S_{SYN} is logical "1," and it is passed to BDC control when the status of S_{SYN} is logical "0" as depicted in Fig. 8. Thus, GVSC and BDC, respectively perform MPPT of PV array under GCM and IDM.

E. Presented eFOGI-FLL Structure

The block diagram of developed eFOGI-FLL is depicted in Fig. 9 where fundamental $\alpha\beta$-axes grid voltages are deduced as follows:

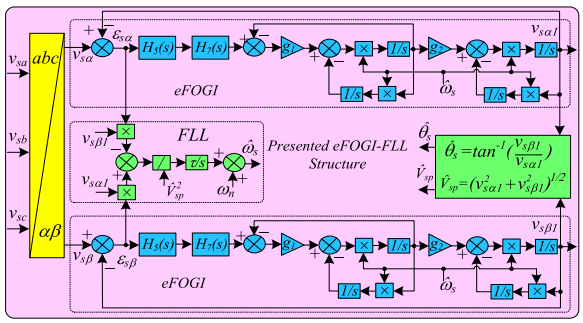

Fig. 9. Block diagram of presented eFOGI-FLL structure.

$$v_{s\alpha 1}(s) = \frac{H_5\, H_7\, g_1\, g_2\, \hat{\omega}_s^2\, s^2}{s^4 + \hat{\omega}_s g_1 s^3 + (2 + H_5 H_7 g_1 g_2)\hat{\omega}_s^2 s^2 + \hat{\omega}_s^3 g_1 s + \hat{\omega}_s^4} v_{s\alpha}(s) \tag{24}$$

$$v_{s\beta 1}(s) = \frac{H_5\, H_7\, g_1\, g_2\, \hat{\omega}_s^2\, s^2}{s^4 + \hat{\omega}_s g_1 s^3 + (2 + H_5 H_7 g_1 g_2)\hat{\omega}_s^2 s^2 + \hat{\omega}_s^3 g_1 s + \hat{\omega}_s^4} v_{s\beta}(s) \tag{25}$$

where $v_{s\alpha 1}$, $v_{s\beta 1}$ are fundamental $\alpha\beta$-axes grid voltages, while $v_{s\alpha}$, $v_{s\beta}$ are $\alpha\beta$-axes grid voltages. On the basis of $v_{s\alpha 1}$, $v_{s\beta 1}$ and error signals ($\varepsilon_{s\alpha}$, $\varepsilon_{s\beta}$), the amplitude, phase-angle and frequency of grid voltages are deduced as follows:

$$\hat{V}_{sp} = \left(v_{s\alpha 1}^2 + v_{s\beta 1}^2\right)^{1/2} \tag{26}$$

$$\hat{\theta}_s = \tan^{-1}(v_{s\beta 1}/v_{s\alpha 1}) \tag{27}$$

$$\hat{\omega}_s = \omega_n + \frac{\tau}{V_{sp}^2} \int \left(\varepsilon_{s\beta} v_{s\alpha 1} - \varepsilon_{s\alpha} v_{s\beta 1}\right) dt \tag{28}$$

where ω_n is nominal grid frequency, and $\varepsilon_{s\alpha}$, $\varepsilon_{s\beta}$ are given as follows:

$$\varepsilon_{s\alpha} = (v_{s\alpha} - v_{s\alpha 1})\ ;\ \varepsilon_{s\beta} = (v_{s\beta} - v_{s\beta 1}). \tag{29}$$

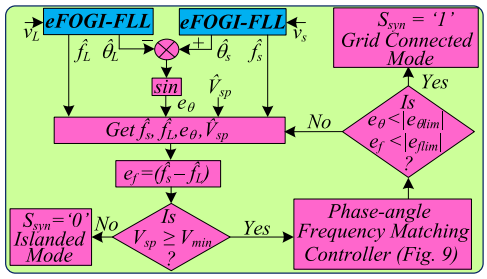

Fig. 10. Presented eFOGI-FLL-based synchronization scheme.

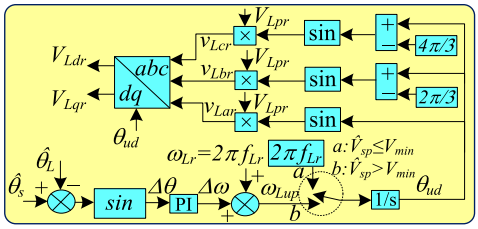

Fig. 11. Phase-angle and frequency matching controller.

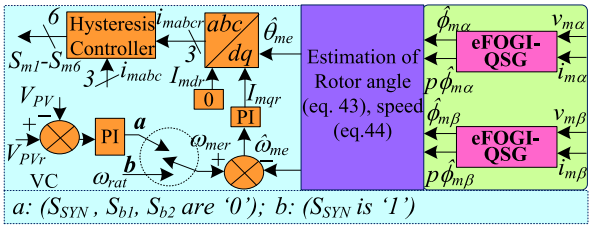

Fig. 12. eFOGI-QSG-based PMSM self-sensing control.

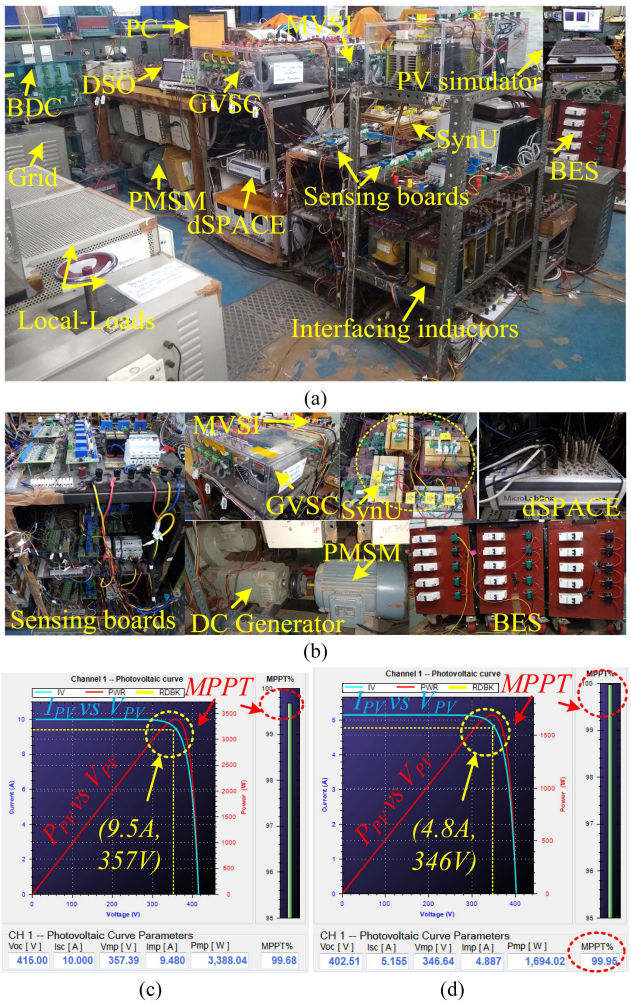

Fig. 13. (a) Test bench. (b) Major system components along with PV array curve at (c) 1 and (d) 0.5 kW/m^2.

Similarly, the phase-angle, frequency and amplitude of load-voltage are estimated by using presented eFOGI-FLL. These estimated parameters of grid and load voltages are then used to implement control for reconnection of grid with WPS as described in Section III-D.

F. eFOGI-FLL Based Synchronization of WPS to Grid

The presented eFOGI-FLL-based control for synchronization of WPS with the utility grid is provided in Fig. 10, wherein frequency and phase-angle of both v_L and v_s are estimated by using developed eFOGI-FLL. The frequency error, e_f and phase-angle error, e_θ, are then evaluated. Besides, the value of estimated amplitude of the grid voltage, $\hat{V}_{sp}$ is stored. Firstly, an availability of the grid is checked by comparing $\hat{V}_{sp}$ with $V_{\min}$ where $V_{\min}$ is the prespecified minimum amplitude of the grid-voltage. If $V_{sp} < V_{\min}$, then the WPS is operated in IM, else the execution is transferred to phase-angle and frequency matching controller, which is shown in Fig. 11, wherein load-angle is continuously updated to match it with the grid-angle, thereby minimizing the e_f, e_θ. Thus, updated load-angle, θ_{ud} is given as follows:

$$\theta_{ud} = \begin{cases} \int \omega_{Lup}\, dt & \text{for } \hat{V}_{sp} > V_{\min} \\ \int (2\pi f_{Lr})\, dt & \text{for } \hat{V}_{sp} \leq V_{\min} \end{cases} \tag{30}$$

where ω_{Lup} is the updated angular load-frequency, while f_{Lr} is the rated load-frequency. Based on value of θ_{ud}, the reference three-phase load voltages (v_{Lar}, v_{Lbr}, v_{Lcr}) are calculated as follows:

$$v_{Lar} = V_{Lpr} \sin \theta_{ud} \tag{31}$$

$$v_{Lbr} = V_{Lpr} \sin(\theta_{ud} - 2\pi/3) \tag{32}$$

$$v_{Lcr} = V_{Lpr} \sin(\theta_{ud} - 4\pi/3) \tag{33}$$

where V_{Lpr} is the amplitude of rated load-voltage. Using (31)–(33), reference qd axes load voltages (V_{Lqr}, V_{Ldr}) are deduced as

$$\begin{bmatrix} V_{Lqr} \\ V_{Ldr} \end{bmatrix} = \frac{2}{3} \begin{bmatrix} -\sin\theta_{ud} & -\sin(\theta_{ud}-2\pi/3) & -\sin(\theta_{ud}-4\pi/3) \\ \cos\theta_{ud} & \cos(\theta_{ud}-2\pi/3) & \cos(\theta_{ud}-4\pi/3) \end{bmatrix} \begin{bmatrix} v_{Lar} \\ v_{Lbr} \\ v_{Lcr} \end{bmatrix}. \tag{34}$$

It is noteworthy that the generation of reference load voltages by using θ_{ud} in accordance to (31)–(34) ensures the matching of load-angle, θ_L with the grid-angle, θ_s. Then, the values of

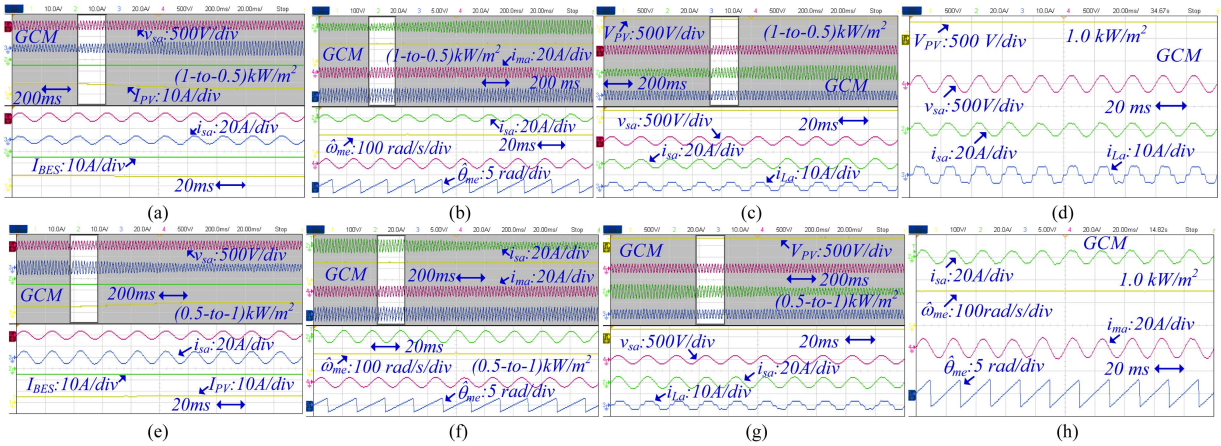

Fig. 14. Test performances of system under GCM for (a)–(c) fall of irradiation, (e)–(g) rise of irradiation, and (d) and (h) steady irradiation.

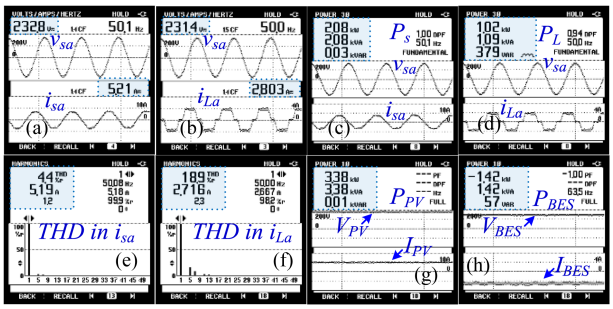

Fig. 15. Test performances depicting values of (a) v_{sa}, i_{sa}, (b) v_{sa}, i_{La}, (c) P_s, (d) P_L, (e) THD of i_{sa}, (f) THD of i_{La}, (g) $P_{\rm PV}$, and (h) $P_{\rm BES}$ under GCM 1 kW/m^2.

e_θ, e_f are checked, and once e_θ, e_f are within specified limits ($e_{\theta\rm lim}$, $e_{f\rm lim}$), the logical high command is provided to SynU, which thereby realizes seamless synchronization of WPS to the utility grid as depicted in Fig. 10. The values of $V_{\rm min}$, $e_{\theta\rm lim}$ and $e_{f\rm lim}$ are selected as 0.95 p.u., 3° and 0.1 Hz as per the IEEE 1547-2018 updated standard [8].

G. eFOGI-QSG-Based PMSM Self-Sensing Control

The $\alpha\beta$-axes model of PMSM ($v_{m\alpha}$, $v_{m\beta}$) ignoring iron-losses and saturation are given as [36], [37]

$$v_{m\alpha} = Lpi_{m\alpha} + Ri_{m\alpha} + p\phi_{m\alpha} \tag{35}$$

$$v_{m\beta} = Lpi_{m\beta} + Ri_{m\beta} + p\phi_{m\beta} \tag{36}$$

where $i_{m\alpha}$, $i_{m\beta}$ and $\phi_{m\alpha}$, $\phi_{m\beta}$ are voltages and rotor-flux linkages in $\alpha\beta$-frame, p is differential operator, and L, R are synchronous inductance and armature resistance. While relationship between rotor-position, θ_{me} and $\phi_{m\alpha}$, $\phi_{m\beta}$ is expressed as follows:

$$\phi_{m\alpha} = \phi_{pm}\cos\theta_{me} \tag{37}$$

$$\phi_{m\beta} = \phi_{pm}\sin\theta_{me} \tag{38}$$

where ϕ_{pm} is PM flux linkages. Using (35)–(38), the derivatives of $\phi_{m\alpha}$ and $\phi_{m\beta}$ are obtained as follows:

$$p\hat{\phi}_{m\alpha} = v_{m\alpha} - Lpi_{m\alpha} - Ri_{m\alpha} = -\phi_{pm}\omega_{me}\sin\theta_{me} \tag{39}$$

$$p\hat{\phi}_{m\beta} = v_{m\beta} - Lpi_{m\beta} - Ri_{m\beta} = \phi_{pm}\omega_{me}\cos\theta_{me} \tag{40}$$

where "^" denotes estimated entities, and ω_{me} is the rotor-speed. Based on (39) and (40), the rotor flux-linkages are estimated as follows:

$$\hat{\phi}_{m\alpha} = \int (v_{m\alpha} - Lpi_{m\alpha} - Ri_{m\alpha})\,dt = \int \hat{e}_{m\alpha}\,dt \tag{41}$$

$$\hat{\phi}_{m\beta} = \int (v_{m\beta} - Lpi_{m\beta} - Ri_{m\beta})\,dt = \int \hat{e}_{m\beta}\,dt. \tag{42}$$

Based on (37) and (38), the rotor angle is estimated as follows:

$$\hat{\theta}_{me} = \tan^{-1}(\hat{\phi}_{m\beta}/\hat{\phi}_{m\alpha}). \tag{43}$$

The differentiation of (43) estimates rotor speed as follows:

$$\hat{\omega}_{me} = \left(\hat{\phi}_{m\alpha}\,p\hat{\phi}_{m\beta} - p\hat{\phi}_{m\alpha}\,\hat{\phi}_{m\beta}\right) / \left(\hat{\phi}^2_{m\alpha} + \hat{\phi}^2_{m\beta}\right). \tag{44}$$

It is worth noting that the $\alpha\beta$-axes components of rotor flux along with the respective derivative components are estimated through eFOGI-QSG structure as noticed from Fig. 12. Then, the rotor position and speed are obtained as per (43) and (44), respectively. Besides, the popular vector control is used to regulate PMSM speed as depicted in figure.

IV. Results and Discussion

Fig. 13(a) illustrates laboratory prototype of WPS where main parts of system like battery storage, GVSC, MVSI, PMSM, dc generator, dSPACE-1202, sensing boards, and SynU are shown in Fig. 13(b). The PV array is emulated by using the PV simulator, and hence, PV curves at 1 and 0.5 kW/m^2 are depicted in Fig. 13(c) and (d) where a reasonable high value of MPPT efficiency, that is more than 99%, is observed. While 1202-dSPACE is used to implement presented control methods in real-time. Meanwhile, LEM-type current and voltage sensors are utilized for sensing relevant current/voltage. Besides, test performances are acquired by using a digital signal oscilloscope and power quality analyzer. In following subsections, experimental behaviors of WPS in GCM, IM and grid synchronization are obtained and reported.

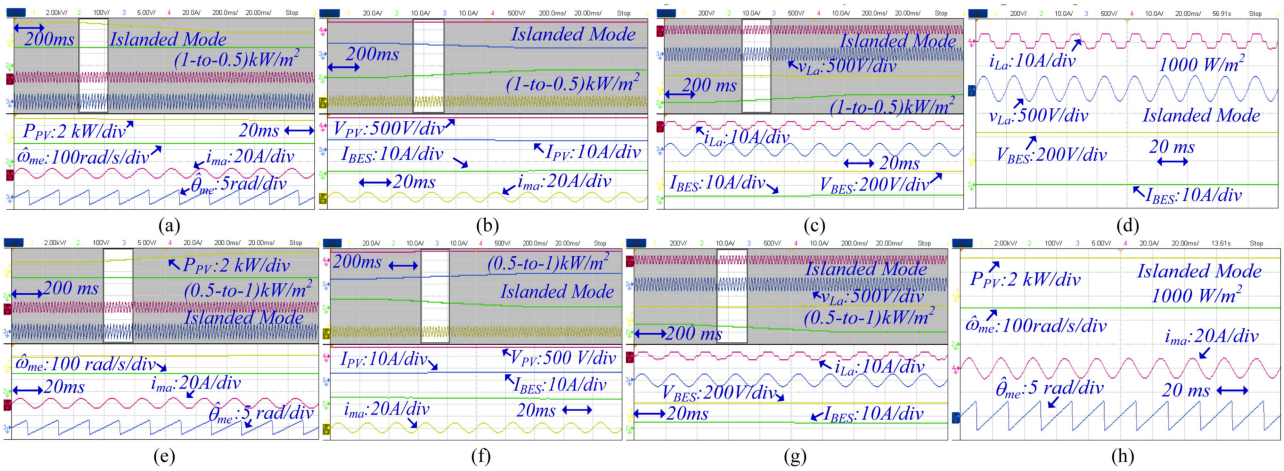

Fig. 16. Test performances of system under IDM for (a)–(c) fall of irradiation, (e)–(g) rise of irradiation, and (d) and (h) steady irradiation.

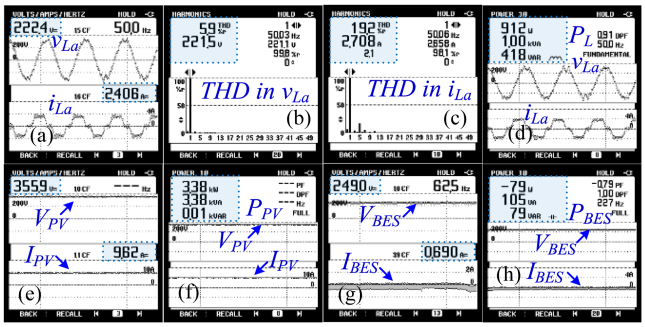

Fig. 17. Test performances depicting values of (a) v_{La}, i_{La}, (b) THD in v_{La}, (c) THD in i_{La}, (d) P_L, (e) $V_{\rm PV}$ and $I_{\rm PV}$, (f) $P_{\rm PV}$, (g) $V_{\rm BES}$ $I_{\rm BES}$, and (h) $P_{\rm BES}$ in IM at 1 kW/m^2.

A. Test Performances in GCM

Test performances of system in GCM for dynamical and steady solar irradiation are illustrated in Fig. 14(a), (b), (c), (e), (f), (g), and (d), (h), respectively wherein the profile of various system indices like i_{sa}, v_{sa}, $I_{\rm BES}$, $V_{\rm PV}$, $I_{\rm PV}$, i_{ma}, ω_{me}, θ_{me}, i_{La}, v_{La} are provided. As the irradiation is decreased, $I_{\rm PV}$ reduces, and hence, i_{sa} increases to support the total load demand. Thus, i_{ma}, $I_{\rm BES}$, and i_{La} remain constant. Similarly, $I_{\rm PV}$ increases, i_{sa} reduces while i_{ma}, $I_{\rm BES}$, and i_{La} remain constant when irradiation increases. Besides, $I_{\rm BES}$ is negative under GCM, which thereby indicates BES charging. Moreover, motor speed along with frequency of both i_{ma} and θ_{me} are constant, which thereby indicates the operation of WPS at constant-speed even during dynamics. In spite of nonsinusoidal i_{La}, the i_{sa} is nearly pure sinusoidal due to the exemplary harmonic filtering capability of eFOGI-QSG as noted from Fig. 14(d). Due to the same reason, an accurate estimation of rotor position and motor speed is acquired as observed from Fig. 14(h). Besides, test performances depicting the values of v_{sa}, i_{sa}, v_{sa}, i_{La}, P_s, P_L, THD of i_{sa}, THD of i_{La}, $P_{\rm PV}$, and$P_{\rm BES}$ in GCM at 1 kW/m^2 are acquired as illustrated in Fig. 15. Even though THD of i_{La} is 18.9%, THD of i_{sa} is merely 4.4% due to the excellent harmonic filtering capability of eFOGI-QSG. Thus, the IEEE-519 standard

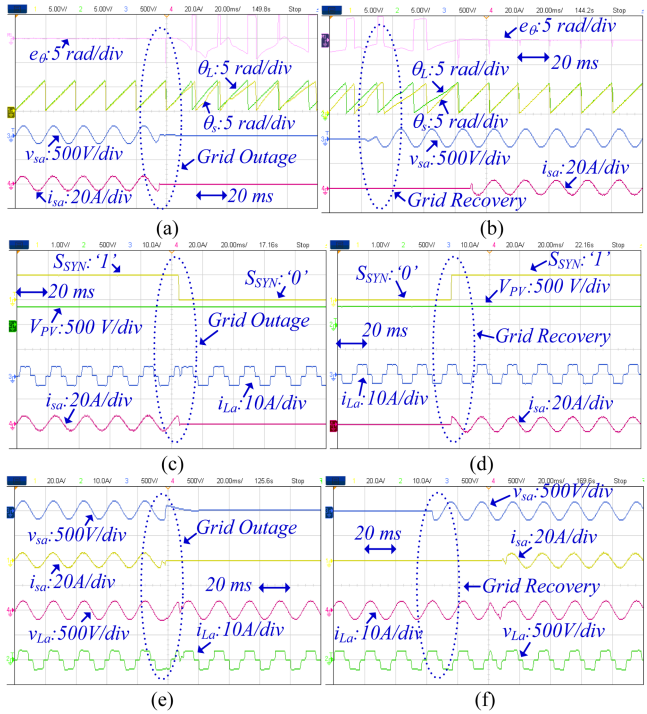

Fig. 18. Test performances of system for seamless mode transition from (a), (c), and (e) GCM to IM, and (b), (d), and (f) IM to GCM. (a) and (b) e_θ, θ_L, θ_s, v_{sa}, and i_{sa}. (c) and (d) $S_{\rm SYN}$, $V_{\rm PV}$, i_{La}, and i_{sa}. (e) and (f) v_{sa}, i_{sa}, v_{La}, and i_{La}.

is also satisfied. Meanwhile, unity power factor is maintained on grid-side, which means that GVSC satisfies the reactive power demand of the load. BES is charged in GCM as indicated by negative sign of P_{BES}. In this mode, total load demand is met by the grid and PV array.

B. Test Performances in Islanded Mode

Test performances of system in IM for dynamical and steady solar irradiance are provided in Fig. 16(a), (b), (c), (e), (f), (g) and (d), (h), respectively, wherein profiles of various system indices like $V_{\rm PV}$, $I_{\rm PV}$, $P_{\rm PV}$, i_{La}, v_{La}, $I_{\rm BES}$, $V_{\rm BES}$, i_{ma}, θ_{me},

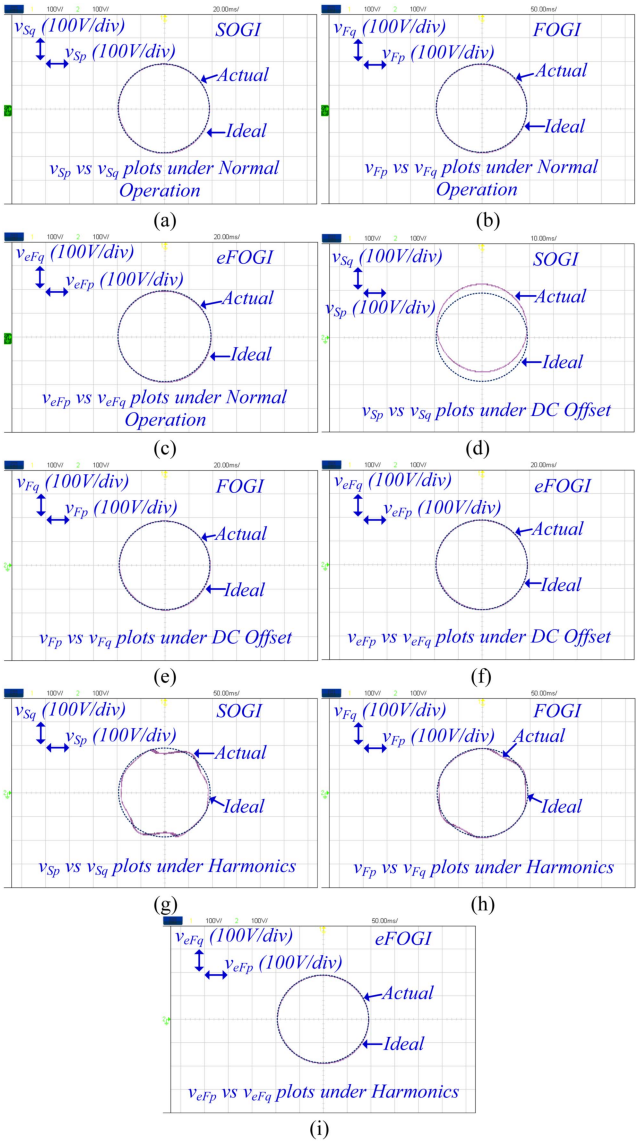

Fig. 19. Test performances of (a), (d), (g) SOGI, (b), (e), (h) FOGI, and (c), (f), (i) eFOGI-based d- and q-axes voltages for operation under (a) and (c) normal condition, (d) and (f) DC-offset, and (g) and (i) harmonics.

ω_{me} are depicted. At 1 kW/m^2, $I_{\rm BES}$ is zero, and thus, PV array feeds both local-loads and PMSM. At irradiation of 500 W/m^2, the two power sources viz. BES and PV array feed total loads. Therefore, i_{ma} and i_{La} are constant at two irradiance values viz. 1 and 0.5 kW/m^2. This implements the uninterrupted operation of the system even under the IM. Despite of non-sinusoidal i_{La}, v_{La} is nearly pure sinusoidal as noted from Fig. 16(d). While an accurate estimation of rotor position and speed is acquired as observed from Fig. 16(h).

Besides, test performances depicting the values of v_{La}, i_{La}, THD in v_{La}, THD in i_{La}, P_L, $V_{\rm PV}$, $I_{\rm PV}$, $P_{\rm PV}$, $V_{\rm BES}$ $I_{\rm BES}$ and $P_{\rm BES}$ in IM at 1 kW/m^2 are provided in Fig. 17(a)–(h). In spite of nonsinusoidal i_{La} with THD of 19.2%, v_{La} is nearly sinusoidal with THD of 5.9% in IM. While values of $I_{\rm PV}$, $V_{\rm PV}$, $P_{\rm PV}$, $I_{\rm BES}$, $V_{\rm BES}$, and $P_{\rm BES}$ are constant as noted from figure. The system is designed such PV array feeds total loads at 1 kW/m^2, and thus $P_{\rm BES}$ is zero at 1 kW/m^2 as noted from Fig. 17(h).

C. Test Performance for Mode Transfer Between GCM and IM

Test performances of the system for seamless mode transition from GCM to IM are depicted in Fig. 18(a), (c), and (e) wherein the profiles of different system parameters like e_θ, θ_L, θ_s, v_{sa}, i_{sa}. v_{La}, i_{La}, $S_{\rm SYN}$, $V_{\rm PV}$ are shown. Under the grid outage, the v_{sa}, and hence the i_{sa} becomes zero, which thereby increases the error between θ_s and θ_L are noted from Fig. 18(a). Thus, the value of S_{SYN} is changed from logical high to logical low as observed from Fig. 18(c). The violation of phase-angle, frequency, and amplitude limits, is the reason behind the change of $S_{\rm SYN}$ status. Subsequently, WPS is disconnected from utility grid, which thereby transfers the operating mode from GCM to IM. Despite of distortion at transition point, both i_{La}, v_{La} maintain their waveshapes in IM [see Fig. 18(e)]. Thus, the uninterrupted operation of the system for seamless mode transition from GCM to IM is implemented.

Besides, test performances for seamless mode transition from IM to GCM illustrating profiles of e_θ, θ_L, θ_s, v_{sa}, i_{sa}. v_{La}, i_{La}, $S_{\rm SYN}$, and $V_{\rm PV}$ are provided in Fig. 18(b), (d), and (f). When the grid is recovered, synchronization control calculates phase-angle, frequency, and voltage errors. When limits on frequency, and voltage are met, a large phase-angle error exists. Such an error is minimized by using a phase-angle matching controller wherein the load-angle is continuously updated to match it with the grid-voltage angle as depicted in Fig. 18(b). As soon as phase-angle error reaches within its limiting value, the level of $S_{\rm SYN}$ is changed from logical low to logical high, which enables supply of three-phase grid currents as observed in Fig. 18(d). This implements the seamless mode transition of the system from IM to GCM. The change in system parameters at the transition point is noted from these figures. Besides, i_{La}, v_{La} maintain their shape even after mode transition as noticed from Fig. 18(f). Thus, the uninterrupted operation of the system is implemented even in IM by realizing seamless mode transfer from IM to GCM.

D. Test Performance Demonstrating Benefits of Presented eFOGI-FLL Over Existing Methods

To illustrate dc-offset and selective harmonic rejection capabilities of eFOGI-FLL, test performances are obtained and a comparison is made with SOGI and FOGI-based FLLs. An investigation of these performances is provided as follows.

Test performances depicting voltage trajectories of SOGI, FOGI and presented eFOGI are obtained as shown in Fig. 19. The d- versus q-axes voltage plots under normal operation, dc-offset and harmonics are illustrated in Fig. 19(a)–(c), (d)–(f) and (g)–(i), respectively. For normal operation, both the real and ideal voltage trajectories are circular and perfectly match for three methods as noticed from Fig. 19(a)–(c). However, voltage trajectory for SOGI is shifted along q-axis under dc-offset as noted from Fig. 19(d). The reason for this drawback is that SOGI does not eliminate dc-offset from its q-axis voltage. While real and ideal voltage trajectories for both FOGI and presented

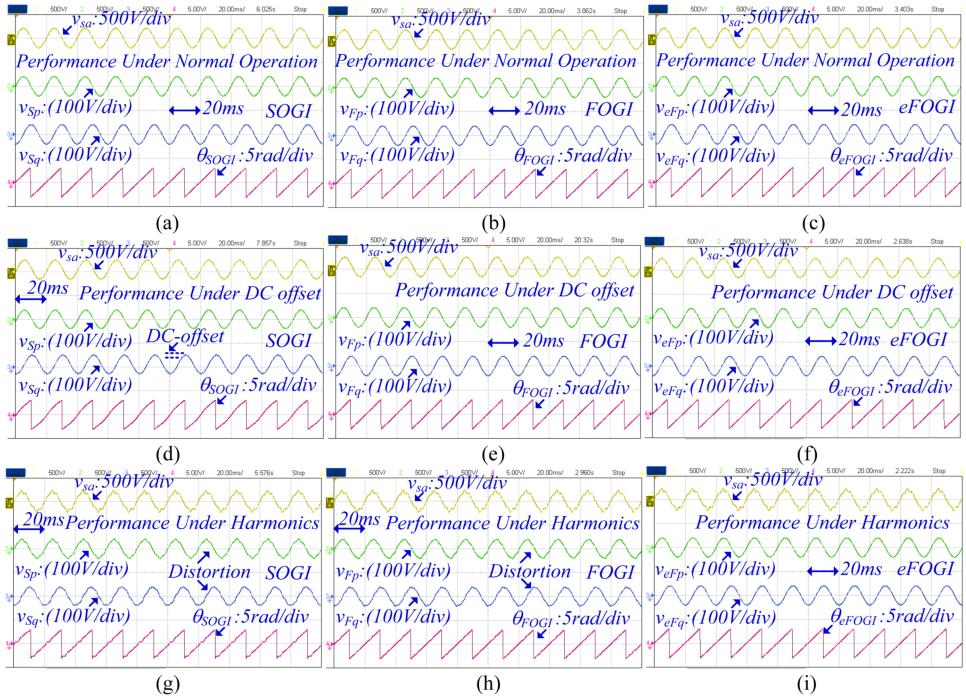

Fig. 20. Test performances of (a), (d), (g) SOGI, (b), (e), (h) FOGI, and (c), (f), (i) eFOGI illustrating input voltage, *d*-axis voltage, *q*-axis voltage, estimated phase angle for operation under (a) and (c) normal condition, (d) and (f) DC-offset, and (g) and (i) harmonics.

eFOGI coincide even under dc-offset as shown in Fig. 19(e) and (f). This indicates that both FOGI and presented eFOGI are immune to dc-offset. On other hand, the real voltage trajectories of both SOGI and FOGI deteriorate under harmonics as noticed from Fig. 19(g) and (h), respectively. The absence of selective harmonic elimination from both SOGI and FOGI is a reason behind their poor performance. While actual voltage trajectory of presented eFOGI is circular and it matches with its corresponding ideal curve under harmonics. The reason for this characteristic is realization of selective harmonic elimination in presented eFOGI. Thus, presented eFOGI continues to provide a good estimate of both the *d*-axis and *q*-axis voltages even when harmonics are present in input voltage.

Test performances depicting variation of input voltage, *d*-axis voltage, *q*-axis voltage and estimated phase angle for SOGI, FOGI and presented eFOGI under normal operation, dc-offset and harmonics are depicted in Fig. 20(a)–(c), (d)–(f), and (g)–(i), respectively. The three methods give nearly pure sinusoidal estimation of both the *q*- and *d*-axes voltages under normal operation as noted from Fig. 20(a)–(c). Consequently, the estimated phase-angle is also smooth. However, dc-offset appears in SOGI-based *q*-axis voltage, and thus, SOGI estimates distorted phase-angle under dc-offset as noted from Fig. 20(d). Meanwhile, both FOGI and eFOGI continue to estimate nearly pure sinusoidal qd-axes voltages even under dc-offset, and hence, the phase-angle estimated by both FOGI and eFOGI is smooth as noticed from Fig. 20(e) and (f). On the other hand, both SOGI and FOGI estimate distorted *qd*-axes voltages under harmonics, and consequently the phase-angle estimated by them is distorted as noted from Fig. 20(g) and (h), whereas presented eFOGI continues to estimate nearly pure sinusoidal *qd*-axes voltages even under harmonics, and thus, eFOGI provides a smooth estimation of phase-angle even when harmonics are present in input voltage as noted from Fig. 20(i). The reason for this feature is a realization of selective harmonic elimination in presented eFOGI. It is to be noted that a comparison of presented eFOGI with both SOGI and FOGI are given in Table IV.

TABLE IV
COMPARISON OF PRESENTED EFOGI WITH FOGI AND SOGI

Parameter	Presented eFOGI	FOGI [23]	SOGI [20]
Attenuation	Absent	Absent	Absent
Phase-shift	Absent	Absent	Absent
DC-offset Rejection	Higher	Lower	Absent
Harmonic attenuation	Higher	Medium	Lower
Selective Harmonic Rejection	Present	Absent	Absent
Computational Burden	Higher	Medium	Lower

V. CONCLUSION

The eFOGI-FLL-based control for synchronization of BES-PV powered WPS to the grid has been presented in this article. It has been shown that presented eFOGI-FLL filters low-order harmonics and dc offset contrary to existing FLLs. The operation of WPS has been realized in IM in event of the grid outage. The eFOGI-FLL has been used to implement grid synchronization of WPS on recovery of the grid, which has enabled GCM. Besides, eFOGI-QSG has been used to develop GVSC control under GCM/IM. The maximum power

control of PV array has also been realized in GVSC control, and thus, PV array has been interfaced across dc-link. This has eliminated a need for a boost converter-based peak power control of PV array. The self-sensing control of PMSM-based eFOGI-QSG is also developed to remove the position sensor. Experimental behavior of WPS at several operating scenarios have been reported to illustrate effectiveness of developed controls.

REFERENCES

[1] The World Bank Group, *Global Photovoltaic Power Potential by Country*, ESMAP Report, WA DC, USA, Jun. 2020.

[2] UN-Water, *UN World Water Development Report: Water and Climate Change*, Paris, France: UNESCO, 2020.

[3] P. Nambisan and M. Khanra, "Optimal energy management of battery supercapacitor aided Solar PV powered agricultural feed mill using Pontryagin's minimum principle," *IEEE Trans. Power Electron.*, vol. 37, no. 2, pp. 2216–2225, Feb. 2022.

[4] A. K. Mishra, B. Singh, and T. Kim, "An efficient and credible grid-interfaced solar PV water pumping system with energy storage," *IEEE J. Photovolt.*, vol. 12, no. 3, pp. 880–887, May 2022.

[5] S. Murshid and B. Singh, "A multiobjective GI-based control for effective operation of PV pumping system under abnormal grid conditions," *IEEE Trans. Ind. Inform.*, vol. 16, no. 11, pp. 6880–6891, Nov. 2020.

[6] S. Shukla and B. Singh, "Single-stage PV-grid interactive induction motor drive with improved flux estimation technique for water pumping with reduced sensors," *IEEE Trans. Power Electron.*, vol. 35, no. 12, pp. 12988–12999, Dec. 2020.

[7] A. K. Mishra and B. Singh, "Grid-integrated SRM-driven solar water pump with power flow management," *IEEE J. Emerg. Sel. Topics Power Electron.*, vol. 9, no. 3, pp. 2723–2734, Jun. 2021.

[8] *IEEE Standard for Interconnection and Interoperability of Distributed Energy Resources with Associated Electric Power Systems Interfaces*, (Revision of IEEE Std 1547-2003), Apr. 2018.

[9] Y. Wang et al., "A forward compensation method to eliminate DC phase error in SRF-PLL," *IEEE Trans. Power Electron.*, vol. 37, no. 6, pp. 6280–6284, Jun. 2022.

[10] Y. Wang, H. Zhang, and W. Hua, "A robust forward compensated type-2 PLL without DC phase error during frequency ramp for embedded magnetic encoder," *IEEE Trans. Power Electron.*, vol. 38, no. 5, pp. 5649–5654, May 2023.

[11] A. K. Verma, C. Subramanian, R. K. Jarial, and P. R.-. Sánchez, "An enhanced discrete-time oscillator-based PLL-less estimation of single phase grid voltage parameters," *IEEE Trans. Ind. Electron.*, vol. 69, no. 4, pp. 3977–3987, Apr. 2022.

[12] H. Pan, Z. Li, and T. Wei, "A novel phase-locked loop with improved-dual adaptive notch filter and multi-variable filter," *IEEE Access*, vol. 7, pp. 176578–176586, 2019.

[13] S. Gautam, W. Xiao, D. D.-C. Lu, H. Ahmed, and J. M. Guerrero, "Development of frequency-fixed all-pass filter-based single-phase phase-locked loop," *IEEE J. Emerg. Sel. Topics Power Electron.*, vol. 10, no. 1, pp. 506–517, Feb. 2022.

[14] S. Zhang, C. Chen, B. Ling, X. Li, D. Lu, and H. Hu, "A generalized harmonic extraction algorithm based on multi-window average filter under synchronous rotating frame," *IEEE Trans. Power Electron.*, vol. 38, no. 3, pp. 3752–3764, Mar. 2023.

[15] S. Lyu, L. Zheng, and J. Song, "A second-order generalized integrator frequency locked loop with damping ratio adaptation," *IEEE Trans. Power Electron.*, vol. 37, no. 3, pp. 2694–2704, Mar. 2022.

[16] X. He, H. Geng, and G. Yang, "A generalized design framework of notch filter based frequency locked loop for three phase grid voltage," *IEEE Trans. Ind. Electron.*, vol. 65, no. 9, pp. 7072–7084, Sep. 2018.

[17] S. Golestan, J. M. Guerrero, J. C. Vasquez, A. M. Abusorrah, and Y. Al-Turki, "Standard SOGI-FLL and its close variants: Precise modeling in LTP framework and determining stability region/robustness metrics," *IEEE Trans. Power Electron.*, vol. 36, no. 1, pp. 409–422, Jan. 2021.

[18] J. Matas, H. Martín, J. de la Hoz, A. Abusorrah, Y. Al-Turki, and H. Alshaeikh, "A new THD measurement method with small computational burden using a SOGI-FLL grid monitoring system," *IEEE Trans. Power Electron.*, vol. 35, no. 6, pp. 5797–5811, Jun. 2020.

[19] C. M. Hackl and M. Landerer, "Modified second-order generalized integrators with Modified frequency locked loop for fast harmonics estimation of distorted single-phase signals," *IEEE Trans. Power Electron.*, vol. 35, no. 3, pp. 3298–3309, Mar. 2020.

[20] S. Golestan, J. M. Guerrero, J. C. Vasquez, A. M. Abusorrah, and Y. Al-Turki, "Modeling, tuning, and performance comparison of second-order-generalized-integrator-based FLLs," *IEEE Trans. Power Electron.*, vol. 33, no. 12, pp. 10229–10239, Dec. 2018.

[21] S. Golestan, J. M. Guerrero, J. C. Vasquez, A. M. Abusorrah, and Y. Al-Turki, "A study on three-phase FLLs," *IEEE Trans. Power Electron.*, vol. 34, no. 1, pp. 213–224, Jan. 2019.

[22] S. Golestan, J. M. Guerrero, J. C. Vasquez, A. M. Abusorrah, and Y. Al-Turki, "Linear time-periodic modeling, examination, and performance enhancement of grid synchronization systems with DC component rejection/estimation capability," *IEEE Trans. Power Electron.*, vol. 36, no. 4, pp. 4237–4253, Apr. 2021.

[23] S. Golestan, J. M. Guerrero, F. Musavi, and J. C. Vasquez, "Single-phase frequency-locked loops: A comprehensive review," *IEEE Trans. Power Electron.*, vol. 34, no. 12, pp. 11791–11812, Dec. 2019.

[24] A. Janabi, B. Wang, and D. Czarkowski, "Generalized Chudnovsky algorithm for real-time PWM selective harmonic elimination/modulation: Two-level VSI example," *IEEE Trans. Power Electron.*, vol. 35, no. 5, pp. 5437–5446, May 2020.

[25] C. Wang, Q. Zhang, D. Chen, Z. Li, W. Yu, and K. Yang, "Application of Newton identities in solving selective harmonic elimination problem with algebraic algorithms," *IEEE J. Emerg. Sel. Topics Power Electron.*, vol. 10, no. 5, pp. 5870–5881, Oct. 2022.

[26] Z. Liu and B. Guan, "Active optimization method for power loss distribution in T-type three-level converter under half-wave symmetry SHEPWM," *IEEE Trans. Ind. Electron.*, vol. 70, no. 10, pp. 9731–9740, Oct. 2023.

[27] M. Sadoughi, A. Pourdadashnia, M. F. Kangarlu, and S. Galvani, "PSO-optimized SHE-PWM technique in a cascaded H-bridge multilevel inverter for variable output voltage applications," *IEEE Trans. Power Electron.*, vol. 37, no. 7, pp. 8065–8075, Jul. 2022.

[28] J. Yang et al., "Identification and stabilization of constant power loads in AC microgrids," *IEEE Trans. Ind. Electron.*, vol. 71, no. 2, pp. 1665–1674, Feb. 2024.

[29] Y. Yang, D. Zhu, D. Zhou, X. Zou, J. Hu, and Y. Kang, "Synchronization instability mechanism and damping enhancement control for DFIG-based wind turbine during grid faults," *IEEE Trans. Power Electron.*, vol. 38, no. 10, pp. 12104–12115, Oct. 2023.

[30] S. Tyagi, B. Singh, and S. Das, "Small hydro based grid forming converter having power sharing and synchronization capability with DFIG based WECS," *IEEE Trans. Ind. Appl.*, vol. 59, no. 4, pp. 5048–5058, Jul./Aug. 2023.

[31] F. S. A. Ismail, "DC Microgrid Planning, Operation, and Control: A comprehensive review," *IEEE Access*, vol. 9, pp. 36154–36172, 2021.

[32] U. Sur, A. Biswas, J. N. Bera, and G. Sarkar, "Holomorphic embedding power flow analysis of hybrid-tidal-farm-integrated power distribution system," *IEEE Syst. J.*, vol. 16, no. 2, pp. 2277–2288, Jun. 2022.

[33] J. G. Ziegler and N. B. Nichols, "Optimum setting for automatic controllers," *Trans. Amer. Soc. Mech. Engineers*, vol. 64, no. 8, pp. 759–768, Nov. 1942.

[34] A. G. Brito, "On the misunderstanding of the Ziegler-Nichols's formulae usage," *IEEE/CAA J. Automatica Sinica*, vol. 6, no. 1, pp. 142–147, 2019.

[35] X. Li, H. Wen, Y. Hu, Y. Du, and Y. Yang, "A comparative study on photovoltaic MPPT algorithms under EN50530 dynamic test procedure," *IEEE Trans. Power Electron.*, vol. 36, no. 4, pp. 4153–4168, Apr. 2021.

[36] A. T. Woldegiorgis, X. Ge, H. Wang, and Y. Zuo, "An active flux estimation in the estimated reference frame for sensorless control of IPMSM," *IEEE Trans. Power Electron.*, vol. 37, no. 8, pp. 9047–9060, Aug. 2022.

[37] Y. Yao, Y. Huang, F. Peng, and J. Dong, "Position sensorless drive and online parameter estimation for surface-mounted PMSMs based on adaptive full-State feedback control," *IEEE Trans. Power Electron.*, vol. 35, no. 7, pp. 7341–7355, Jul. 2020.